

Projected background and sensitivity of AMoRE-II

A. Agrawal , V.V. Alenkov , P. Aryal , J. Beyer , B. Bhandari ,
R.S. Boiko , K. Boonin , O. Buzanov , C.R. Byeon , N. Chanthima ,
M.K. Cheoun , J.S. Choe , Seonho Choi , S. Choudhury ,
J.S. Chung , F.A. Danevich , M. Djamal , D. Drung , C. Enss ,
A. Fleischmann , A.M. Gangapshev , L. Gastaldo , Y.M. Gavriluk ,
A.M. Gezhaev , O. Gileva , V.D. Grigorieva , V.I. Gurentsov ,
C. Ha , D.H. Ha , E.J. Ha , D.H. Hwnag , E.J. Jeon^a , J.A. Jeon ,
H.S. Jo , J. Kaewkhao , C.S. Kang , W.G. Kang , V.V. Kazalov ,
S. Kempf , A. Khan , S. Khan , D.Y. Kim , G.W. Kim , H.B. Kim ,
Ho-Jong Kim , H.J. Kim , H.L. Kim , H.S. Kim , M.B. Kim ,
S.C. Kim , S.K. Kim , S.R. Kim , W.T. Kim , Y.D. Kim ,
Y.H. Kim , K. Kirdsiri , Y.J. Ko , V.V. Kobychiev , V. Kornoukhov ,
V.V. Kuzminov , D.H. Kwon , C.H. Lee , DongYeup Lee ,
E.K. Lee , H.J. Lee , H.S. Lee , J. Lee , J.Y. Lee , K.B. Lee ,
M.H. Lee , M.K. Lee , S.W. Lee , Y.C. Lee , D.S. Leonard ,
H.S. Lim , B. Mailyan , E.P. Makarov , P. Nyanda , Y. Oh ,
S.L. Olsen , S.I. Panasenko , H.K. Park , H.S. Park , K.S. Park ,
S.Y. Park , O.G. Polischuk , H. Prihtiadi , S. Ra , S.S. Ratkevich ,
G. Rooh , M.B. Sari , J. Seo^b , K.M. Seo , B. Sharma , K.A. Shin ,
V.N. Shlegel , K. Siyeon , J. So , N.V. Sokur , J.K. Son , J.W. Song ,
N. Srisittipokakun , V.I. Tretiyak , R. Wirawan , K.R. Woo ,
H.J. Yeon , Y.S. Yoon , Q. Yue 
(AMoRE Collaboration)

¹Address(es) of author(s) should be given
Received: date / Accepted: date

Abstract AMoRE-II aims to search for neutrinoless double beta decay with an array of 423 $\text{Li}_2^{100}\text{MoO}_4$ crystals operating in the cryogenic system as the main phase of the Advanced Molybdenum-based Rare process Experiment (AMoRE). AMoRE has been planned to operate in three phases: AMoRE-pilot, AMoRE-I, and AMoRE-II. AMoRE-II is currently being installed at the Yemi Underground Laboratory, located approximately 1000 meters deep in Jeongseon, Korea. The goal of AMoRE-II is to reach up to $T_{1/2}^{0\nu\beta\beta} \sim 6 \times 10^{26}$ years, corresponding to an effective Majorana mass of 15 – 29 meV, covering all the inverted mass hierarchy regions. To achieve this, the background level of the experimental configurations and possible background sources of gamma and beta events should be well understood. We have intensively performed Monte Carlo simulations using the GEANT4 toolkit in all the ex-

perimental configurations with potential sources. We report the estimated background level that meets the 10^{-4} counts/(keV·kg·yr) requirement for AMoRE-II in the region of interest (ROI) and show the projected half-life sensitivity based on the simulation study.

1 Introduction

The discovery of neutrino oscillations established the existence of massive neutrinos, which is beyond the standard model, and it commands to search the neutrinoless double beta ($0\nu\beta\beta$) decay experimentally to confirm the Majorana nature of neutrinos mediated by non-standard model mechanisms [1, 2].

The inverse of the half-life of $0\nu\beta\beta$ decay, if a light neutrino exchange mediates this process, is proportional to the effective Majorana neutrino mass squared, which is a function of the masses and mixing angles of the three neutrinos and the so-called unknown Majorana

^ae-mail: ejjeon@ibs.re.kr

^be-mail: jeewon.seo.ibs@gmail.com

phases [3–6]. Therefore, the effective Majorana neutrino mass can be obtained from the measured half-life of $0\nu\beta\beta$ decay. The most sensitive lower limits on half-lives of $0\nu\beta\beta$ decay for different isotopes such as ^{76}Ge , ^{82}Se , ^{100}Mo , ^{130}Te , and ^{136}Xe are at 10^{24} to 10^{26} years [7–14].

AMoRE is an experiment searching for $0\nu\beta\beta$ decay using ^{100}Mo isotope in molybdate crystal scintillators operated as cryogenic detectors [15, 16]. It has been planned to operate in three phases: AMoRE-pilot, AMoRE-I, and AMoRE-II. AMoRE-II is the main phase of AMoRE and is currently being installed at the Yemi Underground Laboratory (Yemilab), located approximately 1000 meters deep in Jeongseon, Korea. It uses a 180 kg array of $\text{Li}_2^{100}\text{MoO}_4$ (LMO) crystals, aiming at improving an upper limit on the half-life of $0\nu\beta\beta$ decay of ^{100}Mo up to $T_{1/2}^{0\nu\beta\beta} \sim 6 \times 10^{26}$ years. The sensitivity for $T_{1/2}^{0\nu\beta\beta}$ increases linearly with the experiment exposure if the zero background level in the region of interest (ROI) is achieved. Therefore, the requirements on the background are very severe, and we set AMoRE-II requirements for the background level to be below 10^{-4} counts/(keV·kg·yr) (ckky) in total. Monte Carlo simulations using the GEANT4 toolkit [17] are conducted to assess the background level from all possible sources.

We evaluate the background radiations from radioisotopes in the ^{238}U , ^{232}Th , ^{40}K , and ^{235}U decay chains in detectors, materials in the nearby detector system, shielding materials, and the rock walls surrounding the experimental enclosure. Additionally, we estimate the muon and muon-induced background levels on the AMoRE-II shielding configuration at Yemilab. We discuss the projected half-life sensitivity and an outlook based on simulated background spectra and rates.

2 AMoRE-II experiment

The AMoRE-II experiment is located at Yemilab, approximately 1000 meters deep under Mt. Yemi in Jeongseon, Korea. Yemilab is a newly constructed underground laboratory that involved the excavation of a 782-meter-long tunnel from the 627-meter-long vertical shaft of the Handuk iron mine under Mt. Yemi [18]. The construction of the laboratory was completed in September 2022. The AMoRE experimental hall, the second largest laboratory of Yemilab, is a hexahedron-shaped structure that measures 21 meters in width, 21 meters in length, and 16 meters in height. The preparations for the AMoRE-II experiment are currently underway as a follow-up to the AMoRE-I experiment, which aimed to measure the neutrinoless double beta decay at Yangyang Underground Laboratory (Y2L). The AMoRE-II experiment uses a

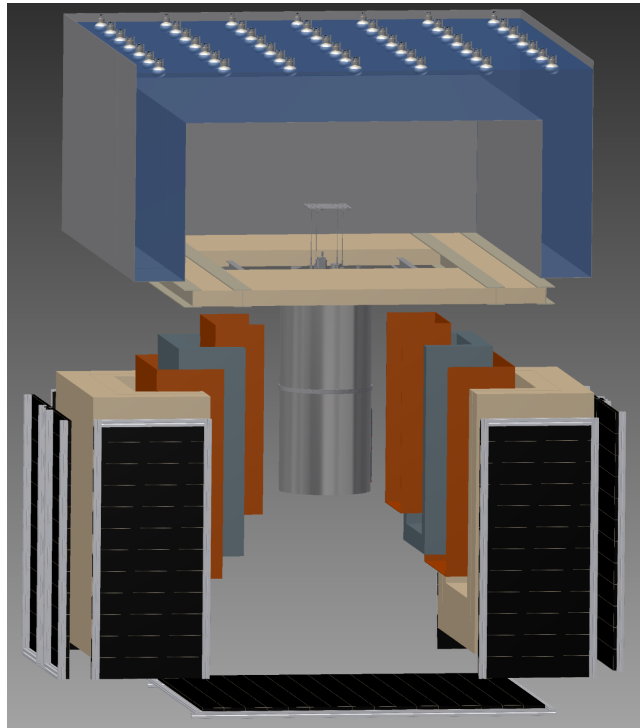


Fig. 1 An overview of AMoRE-II shielding and muon detector system.

423 $\text{Li}_2^{100}\text{MoO}_4$ crystals array kept at cryogenic temperatures. As shown in Fig. 1, the cryostat is surrounded by four shielding layers. The shielding construction is now complete, including plastic scintillator muon veto counters depicted in black colored panels and a water tank that includes photomultiplier tubes (PMTs) installed on the tank ceiling. Below are more detailed descriptions of the experimental setup and detector geometry used in the simulations.

- **Muon detector system**

Based on simulation studies [19, 20], we selected a water tank with a 70 cm thick side structure and an 80 cm thick top structure due to the presence of PMTs. The tank contains approximately 60 tonnes of water and is equipped with 48 PMTs measuring 8 inches/10 inches. It can be played as a shield and an active muon veto detector for the upper part above the cryogenic detector system and shielding layers. The lower part is surrounded by 126 veto counter modules installed like roof tiles overlapping, each consisting of 3 cm thick plastic scintillator panels (PS), as shown in Fig. 1.

- **Shielding structure**

Based on simulation studies [19], we selected a shielding configuration from outside to inward with 70-cm-thick Polyethylene (PE), 1-cm-thick boric acid

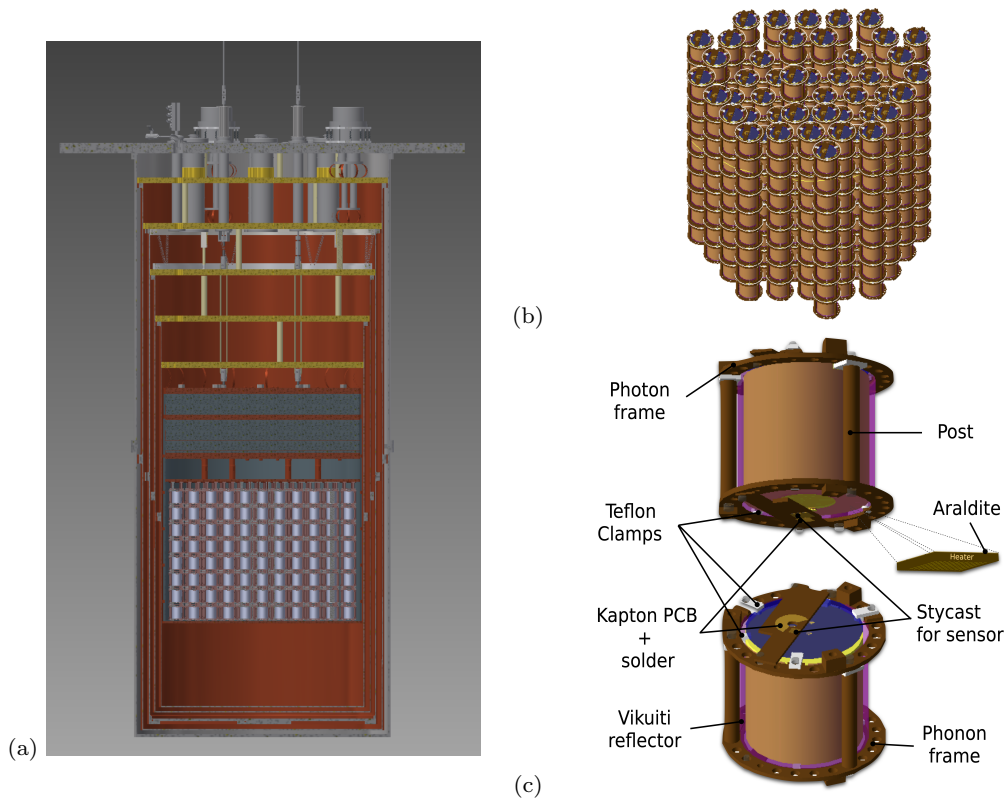


Fig. 2 The detector geometry is shown in clockwise order: (a) Cross-sectional view of the cryostat, (b) Crystal towers, (c) Crystal detector modules.

rubber, 25-cm-thick lead, and 1-cm-thick boric acid powder, as shown in Fig. 1. Boric acid rubber is also installed inside the water Cherenkov detector to prevent the background from thermalized neutrons. A total of ~ 65 tonnes of lead were used for the 25-cm-thick lead shielding. The inner layer of the shielding, which is 5 cm thick out of 25 cm, was made of Boliden lead, which is low-radioactivity modern lead. The other 20 cm lead shield is made of normal lead produced by Nuclear Light Industry Co. Ltd.

• Cryostat

In Fig. 2(a), we present a cross-sectional view of the cryostat. The cryogenic system is installed inside the shielding structure and it consists of five layers of cryostat cans. The layers are arranged from the outside to the inside in the following order: a 5-mm-thick layer made of stainless steel that weighs approximately 1.7 tonnes serves as the outer vacuum chamber (OVC) of the cryostat and four copper shielding layers (50 K, 4 K, 1 K, and 100 mK chambers) with a total thickness of 18 mm. Inside the copper can, the disk-shaped 26-cm-thick low-radioactivity lead structure, the inner lead, is designed to shield the background from entering from the upper part of the

detector. It is supported by 203 kg of copper plates, made of annealed oxygen-free electronic (OFE) copper, not to generate backgrounds that can directly influence the crystal tower. Additionally, a 1-mm-thick superconducting shield layer made of LemerPax lead, an ancient Roman lead with low radioactivity, surrounds crystal detector towers below the inner lead.

• Crystal detector towers and modules

Inside the cryostat, as shown in Fig. 2(b), the crystal detectors consist of 423 modules that are arranged in 47 towers, with each tower comprising nine crystals stacked together. Each crystal is surrounded by a $65\text{-}\mu\text{m}$ -thick Vikuiti enhanced specular reflector film (VM2000) [21, 22] and is assembled into a module using NOSV-grade copper frames with high thermal conductivity and low radioactivity, as shown in Fig. 2(c). The cylindrical crystals are grouped into two sizes: 50 mm diameter for 171 crystals and 60 mm diameter for 252 crystals. The corresponding modules have a diameter of 74 mm and a height of 64.7 mm (84 mm in diameter and 74.7 mm in height). A gold film with a diameter of 1.4 cm and a thickness of 300 nanometers is evaporated on the

bottom surface of the crystal. It serves as a phonon collector thermally connected to a metallic magnetic calorimeter (MMC) [23]. The MMC measures the rise in the crystal temperature caused by radiation absorption [24–27]. A detachable photon detector is installed at the top of the copper frame [28, 29]. It consists of a silicon oxide wafer with a diameter equal to that of the crystal and a thickness of 300 micrometers. This wafer is used as a scintillation light absorber. Each crystal has a stabilization heater on its bottom surface to examine the stability correction with heater pulse [30]. The Araldite adhesive attaches the heater to the crystal surface, and its background contribution is considered in the simulation. The detector module’s wiring system is designed with a Kapton-based flexible printed circuit board (PCB) [31], and the soldering joints are made with pure lead-tin alloy. Although their masses are small, these components are situated near the crystals, and their impact on the background cannot be overlooked and, thus, will be factored into the simulation.

3 Background simulations

3.1 Geant4-based Monte Carlo simulation

We used a Geant4-based simulation framework developed for modeling background spectra of the AMoRE-Pilot and AMoRE-I experiments, which adopted G4 version 10.4.2, implemented AMoRE-specific physics lists for both internal and external background simulations; the Physics list classes of G4EmLivermorePhysics for low energy electromagnetic process, G4RadioactiveDecay for radioactive decay process, QGSP_BERT_HP for high-energy physics process (above 10 GeV), and the precision of the neutron model for neutrons with energies below 20 MeV were used [17, 32, 33]. In addition, we used a full-elastic-scattering dataset for thermal neutrons with energies below 4 eV to precisely describe the shielding effect. Using the simulation framework, we perform simulations for the background contributions from the radioactive decay chains of ^{238}U , ^{232}Th , ^{235}U , and ^{40}K .

We use the energy deposits in the crystals within a 5 ms window to simulate an event like that in the experimental data, considering the 1–2 ms rise times for crystal detectors used in the AMoRE-I experiment [34]. To simulate pileup events resulting from decays with short half-lives, followed by subsequent daughter decay within a few times the typical pulse width (~ 20 – 30 ms) in cryogenic measurements [34], a time window of 100 ms is used. If the second decay happens within 5–100 ms of the first decay, it is excluded from the MC data, similar

to the experimental data. In addition, pileup events can occur due to random coincidences between sources that contribute to ROI. The LMO crystal is a major source of background events, particularly the random coincidence of background events from the two-neutrino double beta ($2\nu\beta\beta$) decay of ^{100}Mo . We also consider its impact on the background contribution to the ROI. More details about this can be found in the following section.

The energy distribution of simulated events was reconstructed by randomly smearing it in a Gaussian shape based on the resolution function obtained from the AMoRE-II R&D setup [35].

3.2 Cosmic muons and muon-induced background

Background caused by cosmic-ray muons is one of the most dangerous external radiation sources. To shield those external radiations, the AMoRE-II detector is positioned around 1000 meters deep under Yemi Mountain and is surrounded by robust shielding materials, as described in Sect. 2.

To investigate the impact of cosmic muons and the induced backgrounds resulting from their interaction with the rocky cavern, shield, and detector materials, we conducted simulations using the muon energy spectrum at Yemilab underground. This spectrum was obtained by digitizing the contour map of the Mt. Yemi area, as detailed in reference [19]. Due to various ambiguities from rock properties, different depths, etc., we used the total muon flux at Yemilab for normalization, which is considered to be 8.2×10^{-8} muons/cm²/s. This value was derived by considering the measured flux at Y2L [36] and the fact that Yemilab is approximately 1.5 times deeper than Y2L. The recent measurement at Yemilab of around 10^{-7} muons/cm²/s is consistent with this value. To account for all secondaries induced by muons traveling through the rocky cavern, we generated muons using a 3-meter-thick rock shell surrounding the cavern. The thickness of the rock shell was optimized based on another simulation. We simulated muons with an energy of 236 GeV, the mean energy of the muon energy spectrum at Yemilab. We estimated the mean energy and event rates of induced neutrons and gammas as a function of the rock thickness and selected the optimal thickness from the plateau in the function line.

In order to estimate background rates for AMoRE-II, we analyzed the neutrons and gamma rays generated by muon interactions with materials in rock, shield, and detector components. The schematic view of the simulation is presented in Fig. 3. Our study involved evaluating different shielding configurations, as described in reference [19]. We compared heavy lead shielding with water tank shielding and ultimately decided to go for

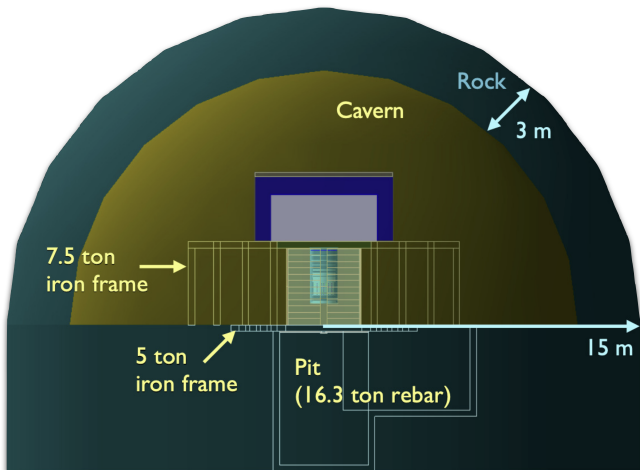


Fig. 3 The overall view of the geometry implemented in the simulation for the AMoRE-II experiment.

lead shielding due to the difficulty of implementing a cryostat in the water shielding. We compared the water Cherenkov detector with the plastic scintillation detector for the part above the cryogenic detector system. Based on simulation studies in reference [20], we opted for a 70-cm-thick water Cherenkov detector with an active muon veto capability. A thorough GEANT4 simulation was conducted to specify the thickness and layers of the various shielding materials. All of those parameters are reflected in the design of the AMoRE-II construction. As a result, we achieved a background rate of 3.1×10^{-6} cky in the (2.8–3.2) MeV energy region when the muon tagging efficiency with both PS and 70-cm-thick water tank is 93.9%.

3.3 Backgrounds from underground environments

The experimental enclosure is surrounded by a rock wall finished with shotcrete. Due to the presence of ^{238}U , ^{232}Th , ^{235}U , and ^{40}K in the rock and shotcrete, this wall is a strong source of γ rays. The rock sample, including shotcrete, is ground and measured by ICP-MS at the Korea Institute of Geoscience and Mineral Resource (KIGAM). The results of the activity measurements are utilized in this paper and will be published, along with measurements of the extensive detector and shielding materials for the AMoRE experiment, in a future publication. Since the estimation of the heavy shielding materials requires significant CPU time, we simulate high-energy gammas from the decay of ^{214}Bi larger than 3 MeV in order to estimate the background rate in the ROI.

Neutrons from (α, n) natural radioactivity reactions in the rock and spontaneous fission, mainly of U atoms,

in the rock are also possible background sources in underground environments. In particular, the thermal neutrons captured by copper or iron in the shield/structure materials generate high energy γ s around 7–8 MeV by (n, γ) reaction. To evaluate the background effect due to these neutrons, we use the neutron flux measured with a Bonner sphere spectrometer system at Y2L [37]. We simulate neutrons by generating them from the rock surface based on the measured energy spectrum.

In addition, as a noble gas, radon is chemically not very reactive and can diffuse easily through many materials infiltrating into the active region of the detectors [38]. One of the most significant isotopes of radon for background considerations is ^{222}Rn , generated from the ^{238}U decay chain in rock walls. Even though its half-life is relatively short ($T_{1/2}=3.82$ d), it contributes to the long-lived isotope ^{210}Pb (22 y). Moreover, several isotopes emitting high-energy gammas are fed by the subsequent decays of ^{222}Rn , as stated in [39]. Specifically, some emissions from decays ^{214}Bi , a descendant of ^{222}Rn decays, have energies over 3 MeV and can produce backgrounds in the $0\nu\beta\beta$ ROI. In order to minimize the effect of radon in the background, laboratories use a radon reduction system (RRS) to supply air with radon levels reduced by at least 1000 times, resulting in 5 Bq/m^3 , the estimated maximum Rn level. Additionally, a vinyl curtain surrounds the shielding structure and is flushed with air containing 5 Bq/m^3 radon. The interior volume between the lead shield and cryostat is reduced by filling it with a urethane nitrogen balloon. We simulate radon background events in the residual air between the OVC and lead shielding to estimate the background rate in ROI. This simulation results in a rate of 1.7×10^{-5} cky.

3.4 Cosmogenic activation

It is potentially dangerous for the AMoRE experiment if there is nuclear decay with a Q-value over 3 MeV inside crystals. To produce crystals with required radiopurity, we used lithium carbonate and $^{100}\text{MoO}_3$ powders with a purity better than 99.998%. We received about 180 kg of enriched molybdenum trioxide powder from Electrochemical Plant JSC [40]. To prevent cosmogenic activation, the material was shipped to Korea by ground and sea. Prior to usage, the delivered powder was kept in a desiccator at Y2L with a temperature of 23°C and a relative humidity of about 10%. There is a 1L/min flow of boil-off gas from a liquid nitrogen dewar to optimize the storage conditions. The molybdenum powder was purified at the Center for Underground Physics (CUP), and purification efficiency and final product radiopurity were checked with HPGe array at CUP (CAGe) and ICP-MS [41–45]. Lithium carbonate precursor was used

from two different sources. One is old stock preserved decades ago at the NIIC, named NRMP TU 6-09-3728-83 [46] and produced at CUP powder [46, 47].

At the AMoRE experimental site in the Yemilab, the rock overburden of approximately 1000 meters significantly reduces the muon flux. As a result, the effect of cosmogenic activation by muons and neutrons is negligible. However, during the crystal production process (includes growing, polishing, cleaning, gold deposition, transportation to Yemilab) at the Earth's surface, crystals are exposed to cosmic rays and may become activated by isotopes with long half-lives, which can contribute to the background. We conducted simulations for all potential radionuclides meeting specific criteria, including origination by spallation from stable nuclides of Mo, Li, and O in the crystal, emission of beta/gamma-rays above 3 MeV, and having a half-live longer than 15 days. We used the ACTIVIA [48] code to calculate radionuclide production rates for 30 days of exposure and 90 days of cooling underground. It found that the production of ^{82}Sr (EC, 180 keV, 25.6 d) / ^{82}Rb (EC, 4400 keV, 1.2 min) in Mo nuclides is most hazardous, with a background level of 10^{-4} ckky. However, the half-life of ^{82}Sr is only 25.6 days. ^{56}Co (EC, 4566 keV, 77.3 d) in Mo is also dangerous, but most of these events are expected to occur within the first year. Hence, increasing the cooling time would help manage the risk associated with this radionuclide. The remaining cosmogenic nuclides are negligible, with a $\sim 10^{-6}$ ckky background level. In addition, we also considered the underground in-situ activation in detector modules, towers, cryostat, and shielding materials, and their impact on background contribution is negligible as below 10^{-6} ckky.

3.5 Backgrounds from the detector system

As detailed in 2, the detector system consists of crystal detector modules, cryostat, and shielding materials. Radiations originating from the LMO crystals are known to be the dominant source of backgrounds. For internal contaminations, radioactive α -decay can be recognized by high-energy peaks in the background spectrum. However, individual alpha peaks resulting from the decays of ^{235}U , ^{238}U , and ^{232}Th partially overlap in the spectrum. Thus, the internal radioactivity of LMO crystals is evaluated using alpha-alpha time-correlated events, as described in Ref. [51]. In this study, we used the upper limit of internal activities obtained by analyzing α energy spectra measured cryogenically using LMO crystals in AMoRE-I at Y2L [34].

Other possible sources are activities from radioisotopes in the ^{238}U , ^{232}Th , ^{235}U , and ^{40}K decay chains

from materials in the nearby crystal detectors, cryostat, and the shielding layers, which produce signals in the crystals. Therefore, this simulation considers all the materials used in the detector components and shielding layers. These materials are scanned with either the High Purity Germanium (HPGe) detectors at Y2L or an Inductively Coupled Plasma Mass-Spectroscopy (ICP-MS) equipment [52]. Several materials are measured in both methods. The activity measurements are listed in Table 1 and are used to normalize the simulation results.

4 Analysis and results

4.1 Event selection

To construct the energy spectra of β/γ background events in the simulations, we applied the same selection cuts used to background data processing in AMoRE-Pilot and AMoRE-I for the selection of $0\nu\beta\beta$ decay event candidates. We consider β/γ events with an assumption of almost 100% α rejection power, based on a discrimination power (DP) of $\sim 10\sigma$ for energies around ROI [35]. It is followed by single-hit selection, α -tagging, and rejection of muon coincidence, which are itemized in the following list.

- We select single-hit β/γ events classified as those with hits in only one of the crystals and none in any of the other crystals to reject background signals resulting from energy deposits in multiple crystals.
- The β/γ events from the decay of ^{208}Tl in the ^{232}Th chain can produce backgrounds in the ROI. However, they can be identified and rejected by using an α -tagging method. This method involves checking for a time correlation with the α signal produced by the preceding $^{212}\text{Bi} \rightarrow ^{208}\text{Tl}$ α decay. We reject the events that occurred within 30 minutes after an α event with 6207 ± 50 keV in the same crystal. This results in a 98% veto efficiency for beta events induced by ^{208}Tl decay with a half-life of 3.05 minutes.
- In order to avoid counting muon coincidence events, we tag muon events with an energy deposit above a set threshold in the plastic scintillator(s) and water tank. Upon examining the time difference between veto hit and crystal hit from the simulation, we found that most muon-tagged events occur within 2 ms. Therefore, we set the veto time window to 5 ms to reject any events occurring within 5 ms following the appearance of a muon-tagged event in the muon veto detectors [20]. As a result, the estimated background

Table 1 Activities and fluxes of the background sources.

Material	Supplier	^{238}U (^{226}Ra) (mBq/kg)	^{232}Th (^{228}Th) (mBq/kg)	Other	Technique
Araldite AW 106 CI	Huntsman	1.7(4)	< 1.0		HPGe
Araldite Hardner, HV953 U CI	Huntsman	2.8(6)	< 1.2		HPGe
Si (heat detector wafer)	Microchemicals	< 2	< 2		HPGe
Stycast 1266 resin	Loctite	< 1.1	< 1.2		HPGe
Stycast 1266 hardener	Loctite	< 1.1	< 3.1		HPGe
Pb/Sn solder (2023)	KNU	< 0.56	< 0.83		HPGe
Ultra-low Pb [49]	Lemer Pax	< 0.05	< 0.05		HPGe
Pb brick	JL Goslar	0.55(17)	0.58(17)	^{210}Pb : 30(1) Bq/kg	CAGE
Pb brick	Boliden	0.48(12)	0.45(11)	^{210}Pb : < 10 Bq/kg	CAGE
Pb brick	Haekgwang	0.38(16)	< 0.25	^{210}Pb : < 180 Bq/kg	CAGE
STS 304 plate	POSCO	1.00(16)	2.36(22)		HPGe
G11	Leiden	2700(200)	906(66)		HPGe
Urethane 0.3 mm	Seokyeong Industry	< 1.2	< 1.4		HPGe
Silicon	HRS Co.	< 0.57	2.1(3)	^{40}K : < 4.9 mBq/kg	HPGe
Boric acid (99.99%)	Alpha Aesar	< 0.46	< 0.50	^{40}K : 98(8) mBq/kg	HPGe
LMO crystal	CUP	0.0020(3)	0.0020(3)	^{235}U : 0.10(4) $\mu\text{Bq/kg}$	AMoRE-I
Material	Supplier	^{238}U (pg/g)	^{232}Th (pg/g)	Other	Technique
PTFE [50]	Maagtechnic	< 9.72	< 9.84		ICP-MS
Vikuiti film (roll type)	3M	< 3.6	< 4.5		ICP-MS
Polyimide-based, HGLS-D211EM	Hanwha L&C	890(90)	< 1.2		ICP-MS
NOSV-Cu post	Aurubis (2021)	0.38(4)	0.97(2)		ICP-MS
NOSV-Cu holder (top & bottom)	Aurubis (2021)	0.32(14)	0.53(21)		ICP-MS
OFE-Cu bulk	Aurubis (2021)	0.83(11)	0.98(14)		ICP-MS
Brass screw	Sanco	0.30(2)	0.89(6)		ICP-MS
Background source	Flux				
Rock gamma	< 10.42 Bq/kg				
Radon air(^{222}Rn)	< 5* Bq/m ³				
Cosmic muons [19]	8.2×10^{-8} muons/cm ² /s				
Radiogenic neutrons [37]	$7.1(10) \times 10^{-6}$ counts/cm ² /s				

The values marked with asterisks (*) correspond to the AMoRE requirements.

Table 2 Simulated components.

AMoRE-II use	Simulated components	Material	Simulated mass (kg)
Module	Heater adhesive	Araldite (AW 106 CI:HV953 U CI = 1:1)	0.0002
	Heater	Si (heat detector wafer)	0.0053
	Reflector	Vikuiti film (roll type)	0.38
	Clamps	PTFE	1
	Kapton PCB	Polyimide-based, HGLS-D211EM	0.09
	Solder for PCB	Pb/Sn solder (2023)	0.09
	Sensor adhesive	Stycast 1266 (resin:hardener=100:28)	0.0002
	Phonon frame	NOSV-Cu holder	26
	Photon frame	NOSV-Cu holder	26
	Post	NOSV-Cu post	23
Screws for module	Brass screw	12	
Cryostat	Cu plate under the inner lead	OFE-Cu bulk	202.76
	Cooling plates supporting rod	G11	4.2
	OVC	STS 304 plate	599.13
	SC lead shield	Ultra-low Pb (Lemer Pax)	51.48
Shielding	Air balloon	Urethane 0.3 mm	6.84
	Inner boric acid shield	Boric acid (99.99%)	243
	Boric acid shield	Silicon and boric acid (99.99%)	1185
	Inner lead shield (1 cm)	Ultra-low Pb (Lemer Pax)	86
	Inner lead shield (25 cm)	Pb brick (JL Goslar)	2055
	Lead shield (5 cm)	Pb brick (Boliden)	10865
	Lead shield (20 cm)	Pb brick (Haekgwang)	53839

rate of cosmic muons is significantly reduced from

1.65×10^{-3} ccky to 2.75×10^{-6} ccky by implementing muon detectors.

4.2 Surface contamination

The decay of surface α on crystals or nearby materials can deposit a range of energies, which can be as high as the Q-value of the decay. Sometimes, this energy falls in ROI. However, it can be distinguished from β/γ signals through pulse shape discrimination (PSD) and the light/heat ratio, with a DP of more than 14 at around 4.785 MeV [35]. Nevertheless, events from the decay of radioactive contaminants in the crystal can pile up through subsequent daughter decay in the decay chains. When analyzing the real data, events that occur sequentially within approximately 2 ms for one crystal are considered indistinguishable. To assess the impact of such events on the background contribution, we carried out a study using beta-alpha pileup events considering a 5 ms time window. These β - α pileup events are from decays of ($^{212}\text{Bi}+^{212}\text{Po}$) in the ^{232}Th decay chain, with a half-life of 294 ns, and decays of ($^{214}\text{Bi}+^{214}\text{Po}$) in the ^{238}U decay chain, with a half-life of 164 μs . Our study found that these events contribute to the continuum down to the ROI region if they occur within the surface depth of the crystal, which is less than 50 μm . The estimated background level of these events is similar to that of β/γ radiation of the crystal in ROI. However, the pileup events can be rejected by approximately 90% within 0.5 ms (as discussed in Sect. 4.3), reducing them to approximately 10^{-6} ckky, which is considered in this study.

In addition, we considered the nearby materials directly facing the crystals, like the copper holder, which houses the crystal and the wafer. The Copper frames and posts are made of NOSV copper, and each post has two screw threads. Despite the surface etching process, the machining process may have left some contamination deeply embedded in the posts, resulting in radioactivity levels more than ten times higher than for NOSV copper. It is considered post-surface contamination, and its background contribution is included in this work.

4.3 Background spectrum and rate in ROI

Figure 4 shows simulated energy spectra with different colors for all possible background sources grouped in categories, which we obtained after applying event selection cuts to the simulated events and convolving them with energy resolution as a function of energy. We categorized the background sources from the detector system into two groups: components located near and far from the crystal. The near-crystal components (G1) include Araldite, bolts, clamps, Stycast, Kapton PCB, heaters, Pb-Sn solder, PTFE, Vikuiti reflector film, and copper materials used in the phonon/photon frame. The

far-crystal components (G2) comprise OVC, Radon, SC-shield, lead shield, and other shielding materials.

In addition, there are other groups of background sources such as crystal internal background, $2\nu\beta\beta$ decay, pileup events, neutrons, muons, and solar neutrinos. The background from interactions of solar neutrinos with the ^{100}Mo target is estimated to be 8.5×10^{-7} ckky at the energy of 3034 keV [53, 54]. This is mainly from single β decay of ^{100}Tc . Electrons emitted in ν_e capture itself, and scattering of ν_e , ν_μ , ν_τ on electrons give much smaller contributions.

The energy spectrum summed over all simulations is shown in Fig. 5 by a solid black line with 1 σ error bars. The background contribution below 3 MeV is mainly from $2\nu\beta\beta$ decay, which is expected due to the use of purified materials.

The high-energy spectrum in the extended ROI ranging from 2.95 to 3.15 MeV is shown in Fig. 6 (a), where the main contributions are from the background sources of ^{214}Bi in the ^{226}Ra - ^{210}Pb decay sub-chain of ^{238}U and ^{208}Tl in the ^{228}Th - ^{208}Pb decay sub-chain of ^{232}Th .

The peaks at 2978.9, 3000., 3053.9, 3081.8, and 3142.6 keV are attributed to high-energy γ emissions from the decay of ^{214}Bi in far-crystal components (G2), such as a 5-cm thick Boliden lead shield layer, OVC, and radon in the air between them.

To eliminate ^{208}Tl decay events, a vetoing process is employed 30 minutes after the 6.2 MeV α precursor as the α -tagging method. However, when dealing with backgrounds from ^{208}Tl decay in materials located near-crystal components (G1), such as Pb-Sn solder and Kapton PCB, the precursor α may not provide an energy level of 6.2 MeV. It can lower veto efficiency and result in background contributions in ROI.

In addition, another background contributor to ROI is pileup events due to the random coincidence of two ^{100}Mo $2\nu\beta\beta$ decay events. We investigated the rate of this background using the DECAY0 program [55] to produce ^{100}Mo $2\nu\beta\beta$ decay events. The estimated background rate within the ROI, which occurred randomly within a 1 ms time window, was 1.2×10^{-4} ckky for 310 g of $^{40}\text{Ca}^{100}\text{MoO}_4$ [56]. Furthermore, we found that a single $2\nu\beta\beta$ decay that coincides randomly with other background sources has an upper limit of 1.1×10^{-4} ckky in ROI. To reduce the background level, we studied rejection efficiency for pileup events [24] and further developed it to meet the AMoRE-II background requirement in a separate work by utilizing various PSD parameters as input parameters for the Boosted Decision Tree (BDT) method. We found that it is possible to reject approximately 90% of pileup events within 0.5 ms, resulting in a background rate of 2.4×10^{-5} ckky for a 6 cm diameter LMO crystal, which includes a single $2\nu\beta\beta$

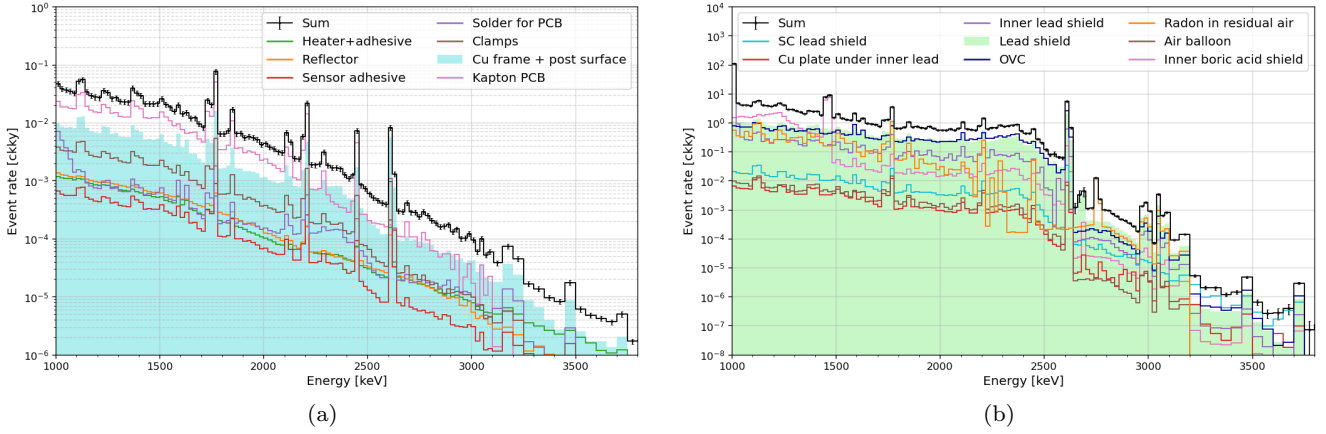


Fig. 4 Backgrounds from different components in the AMoRE-II setup: (a) G1 and (b) G2.

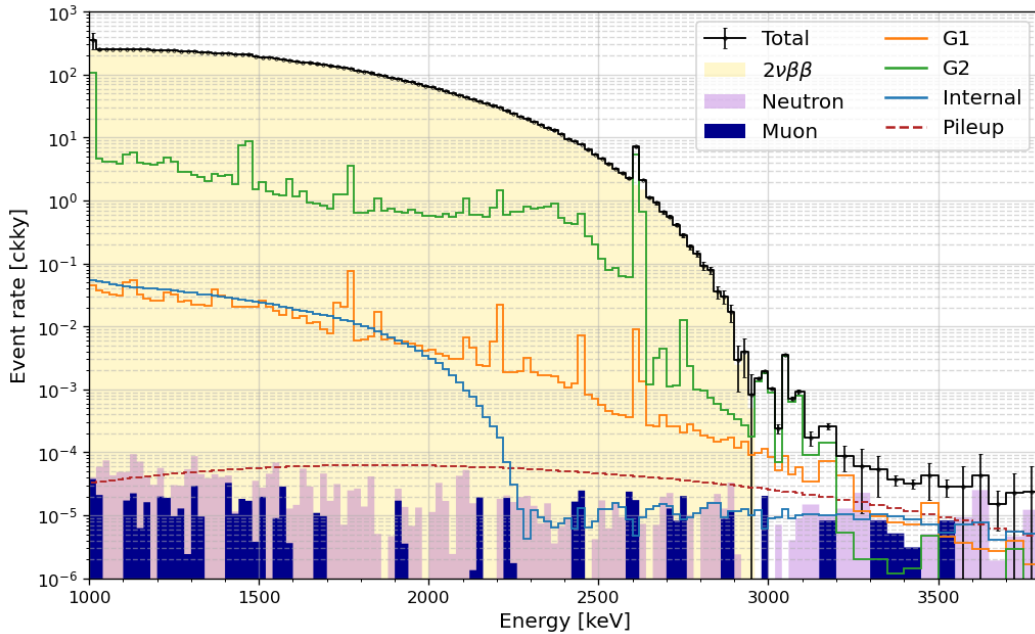


Fig. 5 Summed main components of the background spectrum.

decay that randomly coincides with other background sources. This information is used in this paper.

The background contribution in the (3024–3044) keV range (ROI) of each background source included in the group is shown in Fig. 6 (b). A bar graph represents the background rate by a conservative limit. Meanwhile, the filled circle with error bars is estimated based on the impurity measurement. One of the primary sources of background radioactivity is ^{214}Bi , which is found in the ^{226}Ra – ^{210}Pb decay sub-chain of ^{238}U located in the lead shielding’s innermost layer. The inner 5 cm of current shielding with Boliden lead will be replaced by lead with lower ^{226}Ra contamination.

The detailed results estimated in the ROI of the radioactive sources considered in this study for the back-

ground contributions from radioisotopes in the decay chains of the ^{238}U and ^{232}Th are summarized in Table 3. The summary table also includes evaluations of other background groups such as internal, $2\nu\beta\beta$, neutrons, muons, and solar neutrinos. The total estimated background level is 2.01×10^{-4} ckky. Additionally, the study assessed the background effects of other radioisotopes, such as ^{235}U , ^{40}K , and ^{210}Pb , and found that they have negligible contributions.

5 Estimation of half-life sensitivity

To study the sensitivity of the half-life of $T_{1/2}^{0\nu\beta\beta}$, taking into account the background spectra estimated in Sect. 4.3, we generate ten thousand pseudo-experiments

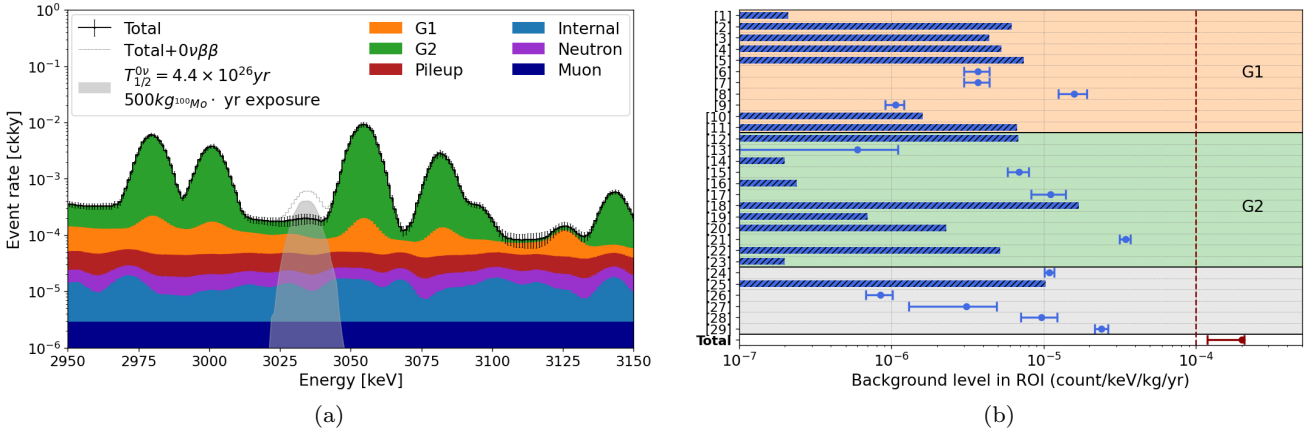


Fig. 6 Background spectrum in the extended ROI (a) and the rate in the ROI (b).

Table 3 Summary of the background event rates in the ROI for the major components.

	No.	Components	Background event rate ($\times 10^{-5}$ ckky)		
			$^{238}\text{U}(^{226}\text{Ra})$	$^{232}\text{Th}(^{228}\text{Th})$	Total
Near component (G1)	1	Heater adhesive	0.006(1)	< 0.015	< 0.021
	2	Heater	< 0.09	< 0.53	< 0.62
	3	Reflector	< 0.20	< 0.24	< 0.44
	4	Clamps	< 0.13	< 0.40	< 0.53
	5	Kapton PCB	0.73(37)	< 0.01	< 0.74
	6	Phonon frame	0.05(4)	0.32(6)	0.37(7)
	7	Photon frame	0.002(1)	0.37(7)	0.37(7)
	8	Post (surface)	0.29(18)	1.30(29)	1.59(34)
	9	Screws for module	0.005(4)	0.101(15)	0.106(15)
	10	Sensor adhesive	< 0.05	< 0.11	< 0.16
	11	Solder for PCB	< 0.03	< 0.64	< 0.67
Far component (G2)	12	SC lead shield	< 0.35	< 0.33	< 0.68
	13	Cu plate under the inner lead	0.05(4)	0.010(8)	0.06(5)
	14	Inner lead shield (1 cm)	< 0.021	< 0.0003	< 0.02
	15	Inner lead shield (25 cm)	0.68(12)	0.013(1)	0.69(12)
	16	Cooling plates supporting rod	< 0.02*	< 0.004*	< 0.024*
	17	OVC	1.05(26)	0.058(6)	1.11(28)
	18	Radon in residual air			< 1.7
	19	Air balloon	< 0.07	< 0.003	< 0.04
	20	Inner boric acid shield	< 0.23	< 0.003	< 0.23
	21	Lead shield (5 cm)	3.40(28)	0.039(3)	3.44(28)
	22	Lead shield (20 cm)	0.52(4)	< 0.002	< 0.52
	23	Boric acid shield	< 0.015*	< 0.002*	< 0.017*
	Total	24	LMO (internal)	0.08(2)	1.01(7)
25		γ from rock			< 1.03
26		Solar ν			0.085(17)
27		Cosmic muons			0.31(18)
28		Radiogenic neutrons			0.97(26)
29		$2\nu\beta\beta$ random coincidence			2.40(24)
Total			20.06$^{+0.68}_{-8.24}$		

The values marked with asterisks (*) represent the limit of the 90% confidence level.

that are analyzed using a fitting procedure as it is done for the measured data. For a single pseudo-experiment for the null hypothesis, the event rate over energy in a single-hit energy spectrum is generated based on Poissonian fluctuations in each 1 keV energy bin of the

background spectrum for each background source estimated in Sect. 4.3.

We use the signal spectrum of $0\nu\beta\beta$ decay simulated and convolved by the energy-dependent resolution and the background spectrum estimated to fit the pseudo-experiment data by using a log-likelihood method. The

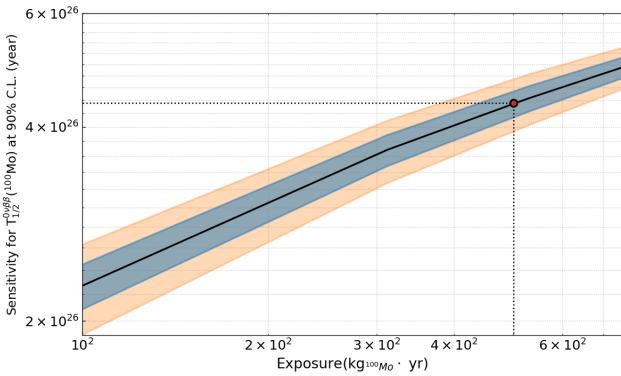


Fig. 7 Median sensitivity of $T_{1/2}^{0\nu\beta\beta}$ as a function of exposure in units of $\text{kg} \cdot \text{year}$, with $\pm 1 \sigma$ ($\pm 2 \sigma$) error band shown in blue (orange).

likelihood function, \mathcal{L} , is given by a binned Poisson likelihood:

$$\mathcal{L} = \prod_i^{N_{bins}} \frac{(\mu_i)^{n_i}}{n_i!} e^{-\mu_i} \quad (1)$$

where n_i represents the number of observed events in the i^{th} energy bin of a pseudo-experiment data and μ_i represents the number of expected events at the same energy bin. μ_i can be obtained by using a model function defined as:

$$\mu_i = S \cdot \mathcal{P}_s(i) + \sum_j B_j \cdot \mathcal{P}_{b_j}(i) \quad (2)$$

where $\mathcal{P}_s(i)$ and $\mathcal{P}_{b_j}(i)$ are the probability density of the models for the signal and the j^{th} background component spectra, respectively, at the i^{th} energy bin, S and B_j represent the number of events in the fitting range of [2950, 3150] keV of the signal and the j^{th} background component spectra. S is expressed in terms of the decay rate of $0\nu\beta\beta$ decay, denoted by $\Gamma^{0\nu}$ as below:

$$\begin{aligned} S &= \epsilon \cdot \Gamma^{0\nu} \cdot N_{100\text{Mo}} \cdot \Delta t \quad (3) \\ &= \epsilon \cdot \frac{\ln 2}{T_{1/2}^{0\nu\beta\beta}} \cdot \frac{N_A}{A_{\text{LMO}}} \cdot a \cdot \mathcal{M} \cdot \Delta t \quad (4) \end{aligned}$$

where ϵ is a detection efficiency of 0.7 [57], N_A is the Avogadro's number, A_{LMO} is the molar mass of $\text{Li}_2^{100}\text{MoO}_4$, a is the concentration of ^{100}Mo , \mathcal{M} is the total detector mass, and Δt is the exposure time. In the fit procedure, $\Gamma^{0\nu}$ and B_j are considered fit parameters.

We obtain the exclusion limit for the half-life of $0\nu\beta\beta$ decay at a 90% confidence level by fitting the model spectrum to pseudo-experiment data. To build the distribution of the half-life limits at a 90% confidence level as a function of exposure in units of $\text{kg}^{100}\text{Mo} \cdot \text{year}$, we generated 10000 pseudo-experiments with a step size of 0.1 years for ten years of exposure time. The median

of the distribution of 90% C.L. half-life limits is shown as a function of exposure in Fig. 7. The blue and orange colors represent the 1 and 2 sigma bands of the median sensitivity, respectively. The half-life limit at 90% C.L. for AMoRE-II with an exposure of $500 \text{ kg}^{100}\text{Mo} \cdot \text{year}$ is estimated to be 4.4×10^{26} years, corresponding to the effective Majorana mass of 18 – 34 meV.

We compared a simulated signal of $0\nu\beta\beta$ decay of ^{100}Mo in the target crystal with the predicted background spectrum using a detector efficiency of 0.7 and an exposure time of 5.2 years. The simulated signal is normalized by the activity corresponding to $T_{1/2}^{0\nu\beta\beta}$ of 4.4×10^{26} years. The results are shown in Figure 6 (a). The dotted grey line represents the sum of the background and signal. We expect this sum to be observed by AMoRE-II after approximately five years of exposure.

6 Conclusions

AMoRE-II uses a 180 kg mass of 423 LMO crystals to improve the limit on the half-life of $0\nu\beta\beta$ decay from ^{100}Mo . In order to achieve the background level of 10^{-4} ckky, Monte-Carlo simulations based on the Geant4 toolkit are intensively conducted. This results in a background level of 2.01×10^{-4} ckky in the ROI. The main source of backgrounds is ^{214}Bi in the ^{226}Ra - ^{210}Pb decay sub-chain of ^{238}U located in the innermost layer of the lead shielding. If required, the background radioactivity can be reduced by substituting the current shielding material with high-purity lead. Taking into account the projected background spectrum and signals from $0\nu\beta\beta$ decay, we estimated the median sensitivity of ^{100}Mo 's $0\nu\beta\beta$ decay half-life limits at a 90% confidence level using pseudo-experiment data. The estimated sensitivity is $(4.4 \pm 0.2) \times 10^{26}$ years ($(4.8 \pm 0.2) \times 10^{26}$ years) with a background level of 2.0×10^{-4} ckky (1.0×10^{-4} ckky) for an exposure of $500 \text{ kg}^{100}\text{Mo} \cdot \text{year}$.

7 Acknowledgement

This research was supported by the Institute for Basic Science (Korea) under project codes IBS-R016-D1 and IBS-R016-A2. It is also supported by the Ministry of Science and Higher Education of the Russian Federation (N121031700314-5), the MEPHI Program Priority 2030.

References

1. W. Rodejohann, Neutrino-less double beta decay and particle physics, International Journal of Modern Physics E 20 (09) (2011) 1833–1930.

2. S. M. Bilenky, C. Giunti, Neutrinoless double-beta decay: A probe of physics beyond the standard model, *International Journal of Modern Physics A* 30 (04n05) (2015) 1530001.
3. R. N. Mohapatra, et al., Theory of neutrinos: a white paper, *Reports on Progress in Physics* 70 (11) (2007) 1757.
4. C. Giunti, C. W. Kim, *Fundamentals of Neutrino Physics and Astrophysics*, 2007.
5. M. Agostini, et al., Toward the discovery of matter creation with neutrinoless double-beta decay, *Rev. Mod. Phys.* 95 (2023) 025002.
6. R. L. Workman, et al., Review of particle physics, *Prog. Theor. Exp. Phys.* (2022) 083C01.
7. S. Abe, et al., Search for the Majorana nature of neutrinos in the inverted mass ordering region with KamLAND-Zen, *Phys. Rev. Lett.* 130 (2023) 051801.
8. M. Agostini, et al., Final results of GERDA on the search for neutrinoless double- β decay, *Phys. Rev. Lett.* 125 (2020) 252502.
9. I. J. Arnquist, et al., Final result of the Majorana Demonstrator's search for neutrinoless double- β decay in ^{76}Ge , *Phys. Rev. Lett.* 130 (2023) 062501.
10. G. Anton, et al., Search for neutrinoless double- β decay with the complete EXO-200 dataset, *Phys. Rev. Lett.* 123 (2019) 161802.
11. D. Q. Adams, et al., Improved limit on neutrinoless double-beta decay in ^{130}Te with CUORE, *Phys. Rev. Lett.* 124 (2020) 122501.
12. O. Azzolini, et al., Final result on the neutrinoless double beta decay of ^{82}Se with CUPID-0, *Phys. Rev. Lett.* 129 (2022) 111801.
13. R. Arnold, et al., Results of the search for neutrinoless double- β decay in ^{100}Mo with the NEMO-3 experiment, *Phys. Rev. D* 92 (2015) 072011.
14. C. Augier, et al., Final results on the $0\nu\beta\beta$ decay half-life limit of ^{100}Mo from the CUPID-Mo experiment, *Eur. Phys. J. C* 82 (2022) 1033.
15. H. Bhang, et al., AMoRE experiment: a search for neutrinoless double beta decay of ^{100}Mo isotope with $^{40}\text{Ca}^{100}\text{MoO}_4$ cryogenic scintillation detector, *Journal of Physics: Conference Series* 375 (4) (2012) 042023.
16. G. Kim, et al., A CaMoO_4 crystal low temperature detector for the AMoRE neutrinoless double beta decay search, *Advances in High Energy Physics* 2015 (2015) 817530.
17. S. Agostinelli, et al., Geant4—a simulation toolkit, *Nuclear Instruments and Methods in Physics Research Section A: Accelerators, Spectrometers, Detectors and Associated Equipment* 506 (3) (2003) 250–303.
18. K. S. Park, et al., Construction of Yemilab, *Front. Phys.* 12 (2024) 1323991.
19. H. Bae, et al., Neutron and muon-induced background studies for the AMoRE double-beta decay experiment, *Astroparticle Physics* 114 (2020) 60–67.
20. J. Seo, E. J. Jeon, M. H. Lee, Estimation of muon induced background event rate of AMoRE-II, *Il Nuovo Cimento* 45 C (23) (Nov. 2022).
21. Vikuiti enhanced specular reflector (ESR). URL <http://multimedia.3m.com/mws/media/193294o/vikuiti-tm-esr-application-guidelines.pdf>.
22. O. Gileva, et al., Thorium and uranium trace ICP-MS analysis for amore project, *Applied Radiation and Isotopes* 194 (2023) 110673.
23. C. Enss, et al., Metallic magnetic calorimeters for particle detection, *Journal of Low Temperature Physics* 121 (2000) 137–176.
24. G. Kim, et al., Novel measurement method of heat and light detection for neutrinoless double beta decay, *Astroparticle Physics* 91 (2017) 105–112.
25. I. Kim, et al., Metallic magnetic calorimeters for particle detection, *Supercond. Sci. Technol.* 30 (2017) 094005.
26. Y.-H. Kim, et al., Superconducting detectors for rare event searches in experimental astroparticle physics, *Supercond. Sci. Technol.* 35 (2022) 063001.
27. H. Kim, et al., Superconducting detectors for rare event searches in experimental astroparticle physics, *Eur. Phys. J. Plus* 138 (2023) 518.
28. H. J. Lee, et al., Development of a scintillation light detector for a cryogenic rare-event-search experiment, *Nuclear Instruments and Methods in Physics Research A* 784 (2015) 508–512.
29. M. B. Kim, et al., Large area light detectors with MMC readouts, *IEEE Transactions on Applied Superconductivity* 33 (2023) 1–5.
30. D. H. Kwon, et al., Stabilization heaters for low-temperature thermal calorimeters, *J. Low. Temp. Phys.* 200 (2020) 312–320.
31. HANWHA L&C Corp, HGLS-D211EM. Tech. rep.
32. J. Allison, et al., Geant4 developments and applications, *IEEE Transactions on Nuclear Science* 53 (1) (2006) 270–278.
33. J. Allison, et al., Recent developments in Geant4, *Nuclear Instruments and Methods in Physics Research Section A: Accelerators, Spectrometers, Detectors and Associated Equipment* 835 (2016) 186–225.
34. H. B. Kim, et al., Status and performance of the AMoRE-I experiment on neutrinoless double beta decay, *Journal of Low Temperature Physics* 209 (5) (2022) 962–970.

-
35. W. Kim, et al., Optimization of cryogenic calorimetric detection with lithium molybdate crystals for AMoRE-II experiments, *Journal of Instrumentation* 17 (07) (2022) P07034.
 36. H. Prihtiadi, et al., Muon detector for the COSINE-100 experiment, *Journal of Instrumentation* 13 (2018) T02007.
 37. Y. S. Yoon, et al., Neutron background measurement for rare event search experiments in the Yangyang underground laboratory, *Astroparticle Physics* 126 (2021) 102533.
 38. J. Martín-Albo, et al., Sensitivity of NEXT-100 to neutrinoless double beta decay, *Journal of High Energy Physics* 2016 (5) (2016) 159.
 39. J. A. Formaggio, C. Martoff, Backgrounds to sensitive experiments underground, *Annual Review of Nuclear and Particle Science* 54 (1) (2004) 361–412.
 40. Electrochemical plant jsc URL <https://www.ecp.ru/eng/>.
 41. S. Park, et al., An enriched ^{100}Mo powder measurement by an array of HPGe detectors, *PosICHEP2018* (2019) 783.
 42. S. Park, et al., Measurement of the background activities of a ^{100}Mo -enriched powder sample for an AMoRE crystal material by using a single High-Purity Germanium Detector, *Journal of the Korean Physical Society* 76 (12) (2020) 1060–1066.
 43. H. Yeon, et al., Preparation of low-radioactive high-purity enriched $^{100}\text{MoO}_3$ powder for AMoRE-II experiment, *Frontiers in Physics* 11 (2023).
 44. O. Gileva, et al., Purification and recovery of $^{100}\text{MoO}_3$ in crystal production for AMoRE experiment, *Journal of Instrumentation* 15 (07) (2020) C07032.
 45. O. Gileva, et al., Investigation of the molybdenum oxide purification for the AMoRE experiment, *J Radioanal. Nucl. Chem.* 314 (3) (2017) 1695–1700.
 46. K. Shin, et al., Selection and purification of Li_2CO_3 precursor for bolometric double beta decay experiments, *Frontiers in Physics* 12 (2024).
 47. O. Gileva, et al., Purification of lithium carbonate from radioactive contaminants using MnO_2 -based inorganic sorbent, *Preprints.org* (September 2023).
 48. J. J. Back, Y. A. Ramachers, ACTIVIA: Calculation of isotope production cross-sections and yields, *Nucl. Instrum. Meth. A* 586 (2008) 286–294.
 49. C. Alduino, et al., The projected background for the CUORE experiment, *The European Physical Journal C* 77 (8) (2017) 543.
 50. E. Aprile, et al., Material radioassay and selection for the XENON1T dark matter experiment, *The European Physical Journal C* 77 (12) (2017) 890.
 51. V. Alenkov, et al., Alpha backgrounds in the AMoRE-Pilot experiment, *Eur. Phys. J. C* 82 (12) (2022) 1140.
 52. O. Gileva, et al., Radioassay of the materials for AMoRE-II experiment, *Front. Phys.* 12 (2024) 1362209.
 53. J. N. Bahcall, et al., Solar models: Current epoch and time dependences, neutrinos, and helioseismological properties, *Astrophys. J.* 555 (2001) 990.
 54. H. Ejiri, S. R. Elliott, Solar neutrino interactions with the double- β decay nuclei ^{82}Se , ^{100}Mo , and ^{150}Nd , *Phys. Rev. C* 95 (2017) 055501.
 55. O. A. Ponkratenko, et al., Event generator DECAY4 for simulating double-beta processes and decays of radioactive nuclei, *Physics of Atomic Nuclei* 63 (7) (2000) 1282–1287.
 56. A. Luqman, et al., Simulations of background sources in AMoRE-I experiment, *Nuclear Instruments and Methods in Physics Research Section A: Accelerators, Spectrometers, Detectors and Associated Equipment* 855 (2017) 140–147.
 57. V. Alenkov, et al., First results from the AMoRE-Pilot neutrinoless double beta decay experiment, *The European Physical Journal C* 79 (9) (2019) 791.